



Cite this: *RSC Adv.*, 2018, 8, 1461

Pressure-driven supercritical CO₂ transport through a silica nanochannel†

Bing Liu, * Xiaoqi Li, Chao Qi, Tingyi Mai, Kaiyun Zhan,* Li Zhao and Yue Shen

A thorough understanding of supercritical CO₂ (scCO₂) transport through nanochannels is of prime significance for the effective exploitation of shale resources and the mitigation of greenhouse gas emission. In this work, we employed the non-equilibrium molecular dynamics simulations method to investigate the pressure-driven scCO₂ transport behavior through silica nanochannels with different external forces and pore sizes. The simulations reveal that the capability of scCO₂ diffusion enhances both in the bulk region and the surface adsorbed layer with the increasing of pressure gradient or nanochannel size, in addition, the slip length increases nonlinearly with the external acceleration or nanochannel width increases and finally reaches a maximum value. The negative slippage occurs at lower pressure gradient or within the narrower nanochannel. Overall, it is the combined effect of strong adsorption, surface diffusion and slippage that causes the nonlinear relation between flow rate and pressure gradient or nanochannel size. The present work would provide theoretical guidance for the scCO₂ enhanced shale oil/gas recovery, CO₂ storage, and mass transport in nanoporous materials.

Received 24th October 2017
 Accepted 16th December 2017

DOI: 10.1039/c7ra11746a

rsc.li/rsc-advances

1. Introduction

Recently, the behaviors of supercritical CO₂ (scCO₂) in narrow pores and confined spaces have attracted extensive attention in the exploration and development of hydrocarbons stored in shale,^{1,2} such as scCO₂ fracturing^{3,4} and injecting.^{5,6} On the other hand, CO₂ injection into tight shales is one of the promising solutions for mitigating carbon emissions^{7,8} and global warming.^{9,10} The nanopores are widely present in shale reservoirs.^{11–14} The basis for scCO₂ geosequestration^{15,16} and enhanced hydrocarbon recovery depends on its unique transport properties induced by the confinement of shale nanopores. The evaluation of scCO₂ enhancing hydrocarbon recovery, enhancement of fracturing efficiency, and estimation of storage capacity require understanding of microscopic behaviors of scCO₂ through shale nanopores, such as adsorption, diffusion and flow.

Confined fluids in nanopores demonstrate microstructural, dynamical and thermophysical behavior that differ significantly from their bulk counterparts due to the molecular asymmetry between fluid–fluid and solid–fluid interactions.¹⁷ This asymmetry leads to inhomogeneous local fluid density distributions, where the superimposition of the attractive potentials from two walls induces confined environments.¹⁸ Extensive molecular simulation studies were reported on CO₂ sorption in the

graphite slit-pores^{18–24} usually treated as the organic matrix of shale reservoirs. In addition, several molecular simulations were addressed on the adsorption structure of CO₂ confined in clay-like^{25,26} and silica^{17,27} slit pores. The results revealed that the nanopore size dramatically influences the adsorption structure of CO₂, which would have potentially significant effects on the transport properties of CO₂ inside the nanopore.²⁸ The diffusion of confined CO₂ obviously weakens as compared with that in bulk fluid^{25,27} and CO₂ diffusion coefficient reduces with the decrease in the pore size.²⁵ The diffusion and migration of CO₂ in silica nanopore occur predominantly along the surface due to hydrogen bonds formed between CO₂ and the surface –OH group.^{27,29} Besides, the widely developed nanopores and ultra-low permeability in shale reservoirs raise concerns on the applicability of Darcy's law to account for mass transport in shale. However, it breaks down for flow through very narrow pores because the continuum flow hypothesis is invalid.^{23,28} Efforts have been made to moderate for the breakdown of Darcy's law *via* gas slippage theory,²³ for example, the Klinkenberg effect.^{30,31} Such empirical corrections can not capture the complex adsorption and transport behavior of the fluid in ultra-confining porous materials.³² Falk *et al.* demonstrated that the non-Darcy behavior results from strong adsorption in kerogen and the breakdown of hydrodynamics at the nanoscale.³² Monteiro *et al.* suggested a hydrodynamic model of gas flow in nanoporous media by introducing a pressure gradient-dependent permeability of kerogen, which obeys power function relationship.³³ Wang *et al.* reported the pressure-driven flow behavior of scCO₂ confined in shale organic nanopores.²⁴ They observed that the streaming velocity profile tends to a plug

School of Science, China University of Petroleum, Qingdao 266580, Shandong, China.
 E-mail: liubing19720115@gmail.com; zhanky@upc.edu.cn

† Electronic supplementary information (ESI) available. See DOI: 10.1039/c7ra11746a



flow and the magnitude far exceeds the prediction of the no-slip Poiseuille equation. Firouzi and Wilcox investigated the gas slippage and Klinkenberg effects of CO₂ confined in carbon slit pores.²³ They reported a plug flow occurs at pore size less than 2 nm, a parabolic velocity profile at pore size larger than 10 nm, and the dramatic underestimation of the CO₂ permeability using the bulk phase viscosity. In summary, the transport of scCO₂ in inorganic nanochannel remains unclear, and there is a strong need for a reliable theoretical framework of scCO₂ transport inside nanoporous matrix due to the constraint of the lowest permeability in the fluid path to the overall permeability of the shale.

Herein, non-equilibrium molecular dynamics (NEMD) simulations were conducted to investigate the pressure-driven scCO₂ transport through the silica nanochannel. The effects of flow driving pressure gradient and nanochannel size on scCO₂ transport were determined by exploring the adsorption, diffusion and flow of scCO₂ molecules. The density profiles and residence autocorrelation functions were employed to describe adsorption. The velocity profiles, the slippage effect, and the flow rate as the function of pressure gradients or nanochannel sizes were applied to characterize the flow behavior.

2. Models and methodology

The nanochannel with the size of $71.60 \times 50.12 \times H \text{ \AA}^3$ was formed by two 10.5 Å cristobalite plates. H denoted the inter-layer space of two plates providing the nanochannel for scCO₂ transport. The silica nanochannels with hydroxylated surfaces³⁴ were fixed in all simulations. Periodic boundary conditions were applied in three dimensions. To obtain saturated adsorption of scCO₂ in nanochannels under 373.15 K and 35 MPa, equilibrium molecular dynamics (EMD) simulations were carried out for 2 ns to get the isothermal adsorption curve³⁵ (ESI Fig. S1†). The initial model was shown in Fig. 1(a).

As applying an acceleration or a force on all atoms directly^{24,36–38} was improper to simulate desorption from surfaces, the whole nanochannel was divided into three segments along X dimension, named G-region, Buffer and S-

region, respectively, as shown in Fig. 1(b). A driving pressure gradient was exerted on the system by applying an acceleration along X direction on scCO₂ molecules in G-region in order to generate the Poiseuille flow through the nanochannel. A bigger acceleration corresponds to a greater pressure gradient. The effect of pressure gradient on transport behavior was examined by altering the acceleration ranged from 0.001 to 0.05 kcal ($\text{\AA}^{-1} \text{ g}^{-1}$) as H is 28.50 Å. The effect of nanochannel sizes on transport behavior was studied by altering H from 7.25 to 50.00 Å as the acceleration is 0.01 kcal ($\text{\AA}^{-1} \text{ g}^{-1}$). All calculations were executed in S-region. The NEMD simulations were performed to simulate mass transport for 6 ns which is enough to obtain a steady scCO₂ flow.

Both the EMD and NEMD simulations were performed using large-scale atomic/molecular massively parallel simulator (LAMMPS)³⁹ software in the NVT ensemble with a time step of 1 fs. Visualization of the dynamics process was carried out using the program VMD.⁴⁰ The Nosé–Hoover^{41,42} thermostat was employed to control the temperature. The silica nanochannel was modeled with the CLAYFF⁴³ force field. CO₂ molecules were described by the three-site EPM2 (ref. 44) model which was successfully demonstrated to reproduce critical point of CO₂ in experiment. All the VDW interactions were described by the 12–6 Lennard-Jones potential. The cutoff of non-bonded interaction was set to be 9.5 Å. Long-range electrostatic interaction was calculated by PPPM⁴⁵ summation method with the accuracy of 0.0001e. The interaction between different types of atoms was determined by the Lorentz–Berthelot rule: $\epsilon_{ij} = \sqrt{\epsilon_i \epsilon_j}$ and $\sigma_{ij} = (\sigma_i + \sigma_j)/2$. All parameters were given in the ESI Table S1.†

3. Results and discussions

3.1 Effect of pressure gradient

3.1.1 Effect of pressure gradient on adsorption of scCO₂. In Fig. 2(a), we presented the density profiles of scCO₂ under different pressure gradients to explore the influence of pressure gradient on adsorption. As shown, the density profiles along Z direction are symmetrical about the central axis of the nanochannel. There are two primary peaks and two secondary peaks

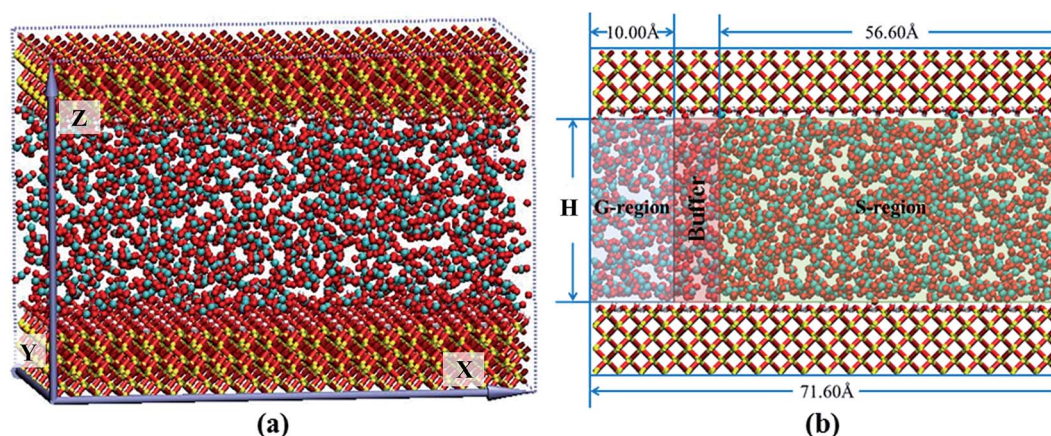


Fig. 1 The MD simulation model: (a) snapshot of simulation model. (b) Schematic images of different region distribution.



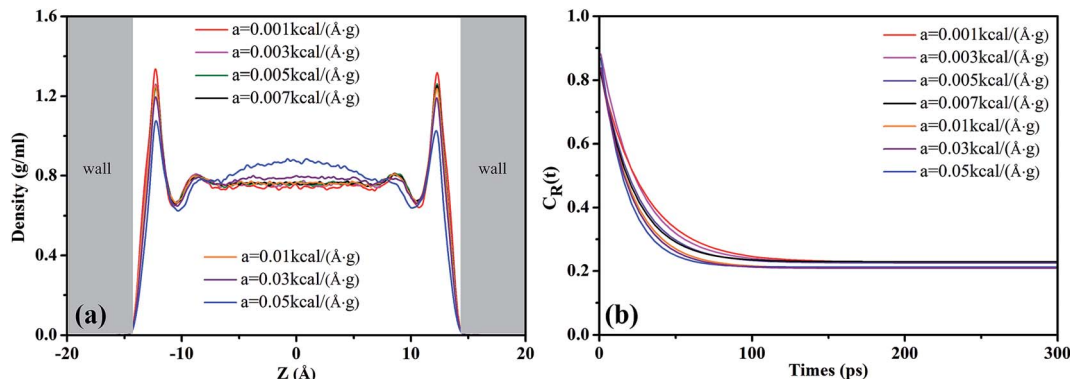


Fig. 2 Adsorption of scCO_2 (a) density profiles of scCO_2 in 28.50 Å SiO_2 nanochannel with external acceleration ranging from 0.001 kcal ($\text{\AA}^{-1}\text{g}^{-1}$) to 0.05 kcal ($\text{\AA}^{-1}\text{g}^{-1}$). (b) The residence autocorrelation function for carbon atoms in the adsorbed layers as a function of time under different acceleration.

appear near the surfaces, indicating that the scCO_2 form four structuring adsorption layers. This shows that the scCO_2 molecules pack more closely near the surface than those far away from the surfaces. The monolayer peak positions are almost independent of pressure gradient, while the second layer peaks shift slightly as the gradient pressure increases and almost disappears at the highest gradient pressure. The density in the center of the channel increases slightly under relatively low pressure gradients while increases obviously at higher pressure gradients. The results indicate that a high pressure gradient dramatically affects the distribution of scCO_2 inside the nanochannel. Under the high pressure gradients, some of adsorbed scCO_2 desorb from the surfaces and enter into the channel central areas. Such behavior could improve the effective permeability⁴⁶ of scCO_2 in channel, which contributes to the scCO_2 flow. However, the shape of the density profiles remains almost unchanged under the lower pressure gradients indicating a little influence on the distribution of scCO_2 , which is in agreement with the results obtained by Kasiteropoulou.⁴⁷

In order to quantify the residence time of scCO_2 molecules remaining near the nanochannel surface, residence autocorrelation function, $C_R(t)$, was calculated by:^{48–50}

$$C_R(t) = \frac{\langle O_w(t)O_w(0) \rangle}{\langle O_w(0)O_w(0) \rangle} \quad (1)$$

where $O_w(t)$ describes whether one scCO_2 molecule is in the first adsorption layer at time t . $O_w(t)$ equals one indicating a scCO_2 molecule within the first adsorption layer. $O_w(t)$ equals zero meaning that a scCO_2 molecule leaves the first adsorption layer. The angular bracket denotes the ensemble average. Carbon atom in scCO_2 is considered to identify the position of one scCO_2 molecule. $C_R(t)$ decays from 1 to 0. The faster decay of $C_R(t)$ implies the shorter time for scCO_2 residing in the first adsorption layer.

The $C_R(t)$ for scCO_2 at the different pressure gradients is shown in Fig. 2(b). $C_R(t)$ decreases faster as pressure gradient increases, implying a shorter residence time of scCO_2 in the adsorption layer at bigger pressure gradients. The high pressure gradients could facilitate the fluid mobility and enhance the

occurrence of molecular collisions, and then driving the adsorbed scCO_2 molecules away from the surface. The $C_R(t)$ plateaus occurs after about 120 ps, indicating that some of the adsorbed scCO_2 molecules are not desorbed within the simulation time because of the electrostatic interaction and the hydrogen bond between scCO_2 and the surface.⁵¹ These scCO_2 molecules that can not be desorbed from the surfaces will reduce the scCO_2 flow in shale reservoirs but benefit the CO_2 sequestration.

3.1.2 Effect of pressure gradient on diffusion coefficient of scCO_2 . The diffusion coefficient is a significant parameter revealing the mechanism of mass transfer. The self-diffusion coefficient can be obtained by Einstein's relation

$$D = \lim_{t \rightarrow \infty} \frac{1}{2dNt} \left\langle \sum_{j=1}^N [r_j(t) - r_j(0)]^2 \right\rangle \quad (2)$$

where r_j is the position vector of the j scCO_2 molecule, d is the dimension of the system, N is the total scCO_2 molecules and the angular bracket represents the ensemble average. In this work, D was calculated for motions in Y and Z dimensions, and hence $d = 2$.

Fig. 3 illustrates the diffusion coefficients of scCO_2 at different pressure gradients and areas in the nanochannel. As

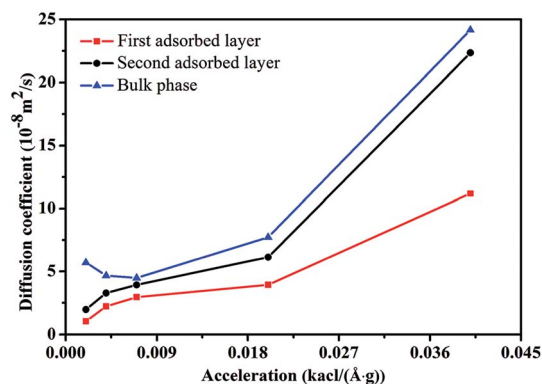


Fig. 3 The diffusion coefficient of scCO_2 molecular in different adsorbed layers with different external accelerations.



pressure gradient increases, the diffusion coefficient of scCO_2 in the adsorption layers increases while it decreases firstly and then rises for bulk scCO_2 . The variation of diffusion coefficients of scCO_2 under lower pressure gradients was mainly affected by the variation in the density distribution. As shown in Fig. 2(a), the density near the surface reduces with the increasing pressure gradient as the acceleration is less than $0.007 \text{ kcal } (\text{\AA}^{-1} \text{ g}^{-1})$. This indicates that the partial pressure in adsorbed layers decreases, leading to the increase of scCO_2 diffusion coefficient. The increasing density of bulk scCO_2 indicates the enhancement of the partial pressure in the central area of nanochannel, resulting in the decrease of scCO_2 diffusion coefficient. In this case, the density distribution plays the dominant role in the diffusibility of scCO_2 within the nanochannel. As the acceleration is greater than $0.007 \text{ kcal } (\text{\AA}^{-1} \text{ g}^{-1})$, the largely undermined adsorption strength with increasing pressure gradient indicates the increase of the scCO_2 velocity within the nanochannel. The raising velocity may lead to the decrease of scCO_2 pressure, which induces the increase of the diffusion coefficient. Herein, the increasing velocity plays the pivotal role in scCO_2 diffusibility inside the nanochannel. As indicated from the Stokes–Einstein relation, the increase in the diffusion coefficient implies the decrease in the viscosity. Therefore, we conclude that such changes could affect the flow of scCO_2 within the nanochannel.

3.1.3 Effect of pressure gradient on flow behavior of scCO_2 .

In Fig. 4(a), we depicted the velocity profiles at different pressure gradients in order to characterize the flow behavior of scCO_2 within the nanochannel. The velocity profiles were obtained by fitting data using the quadratic function:

$$v(z) = az^2 + bz + c \quad (3)$$

where a , b , and c are the fitting parameters describing the flow process, a characterizes the curvature. The larger the absolute value of a is, the steeper the curve and the greater the velocity gradient. c represents the maximum velocity. The fitting parameters were provided in the ESI Table S4.†

In Fig. 4(a), the velocity profiles with the parabolic shape^{24,36,38} are symmetrical about the central axis of the nanochannel. The larger pressure gradients induce the greater

axial velocities and sharper parabolic velocity curves. Moreover, we notice that there are non-zero velocities near the surfaces, which leads to the slippage phenomenon. The slip velocity increases as the pressure gradient increases. Here, we employed the slip length L_s to describe the slippage phenomenon, as defined by⁵²

$$L_s = -\frac{v(z_{\text{surf}})}{(dv/dz)_{z_{\text{surf}}}} \quad (4)$$

where $v(z_{\text{surf}})$ is the slip velocity, v is the velocity profile in the flow direction, and $(dv/dz)_{z_{\text{surf}}}$ is the velocity gradient with respect to z on the surface. Slip length is the distance extrapolated into the surface where the velocity vanishes as supposed by no-slip boundary condition.⁵³ Fig. 4(b) demonstrates the slip lengths for scCO_2 flow in silica nanochannel under different pressure gradients. The inset shows the derivatives of the velocity with respect to z on the surface and the slip velocities. Clearly, a negative slip length^{54–57} occurs as the acceleration is less than $0.004 \text{ kcal } (\text{\AA}^{-1} \text{ g}^{-1})$. The main reason can be explained as follows. Under small pressure gradients, the shear force, as reflected by velocity gradient in the inset in Fig. 4(b), is too small to overcome the attractive interactions between scCO_2 and the surface. This leads to the zero velocity for scCO_2 molecules near the surfaces, indicating the presence of scCO_2 boundary layer whose thickness equals slip length. In this case, adsorbed scCO_2 are trapped on nanochannel surfaces, which is so-called sticking phenomenon,⁵⁸ confining the flow and diffusion of scCO_2 . In addition, the slip length shows a non-monotonous increase with pressure gradients. The increasing pressure gradient promotes scCO_2 flow and detaches scCO_2 molecules from the surfaces due to the enhancement of shear rate, which stimulates surface diffusion⁵⁹ of scCO_2 . Moreover, the rate of increase in slip velocity is greater than that of velocity gradient. Consequently, slip length increases rapidly with increasing pressure gradient. As pressure gradient further increases, the ratio of slip velocity to velocity gradient decreases gradually which cause the slip length increases slowly and reaches a maximum value finally. After that, the velocity of bulk scCO_2 increases much faster than slip velocity with the increase in pressure gradient due to the strong adsorbed potential of the

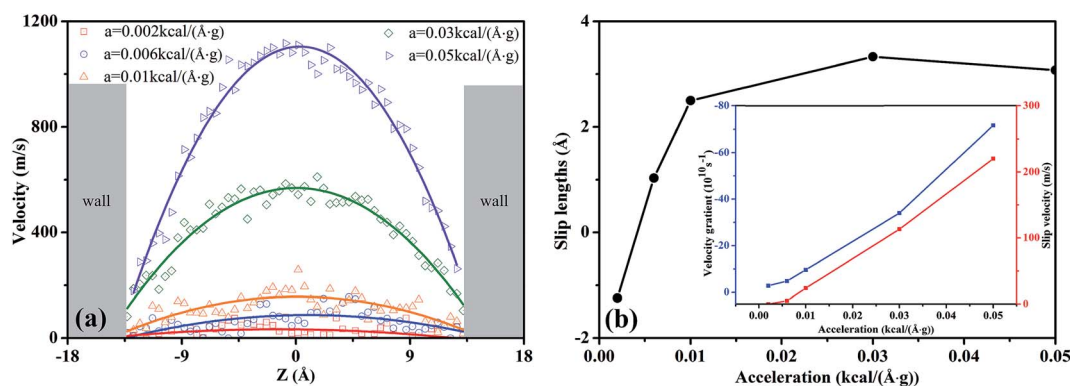


Fig. 4 (a) The effects of external acceleration on the velocity profiles of scCO_2 molecular in nanochannel. (b) Slip length as a function of the external acceleration for scCO_2 molecular.



surfaces. This leads to a large increase in velocity gradient greater than the rate of increase in slip velocity. Therefore, slip length will decrease gradually as pressure gradient increases.

Fig. 5 depicts the scCO_2 flow rate as a function of pressure gradient, revealing a nonlinear relationship different from Darcy's law where permeability is defined as a material property of the rock. This indicates that Darcy's law dramatically fails to describe scCO_2 transport in nanochannel. From the analysis of Fig. 2 and 3 mentioned above, we conclude that the permeability increases and the viscosity decreases as pressure gradient increases. Hence, the ratio of the permeability to the viscosity, *i.e.*, mobility, increases with the increasing of pressure gradient, characterizing the seepage capacity of scCO_2 in nanochannel. It is observed that the mobility is linearly related to pressure gradient shown by the inset in Fig. 5. This corresponds to the hydrodynamic model of gas flow in nanoporous media where permeability is power function of pressure gradient.³³

3.2 Effect of nanochannel width

3.2.1 Effect of nanochannel width on adsorption of scCO_2 .

The density profiles of scCO_2 in different nanochannels were presented in Fig. 6(a), showing the formation of several structuring layers for scCO_2 molecules, which is consistent with previous reports.^{18,24,37,60} For $H = 7.25 \text{ \AA}$, the two symmetrical density peaks indicate that scCO_2 form two primary adsorption layers due to partial superimposition of the attractive potentials from two surfaces.³⁷ Accordingly, the peaks of the density profiles are the highest. As $H = 14.5 \text{ \AA}$, the appearing of two primary peaks and two secondary peaks indicates that there are four adsorption layers form within the nanochannel. This arises from the further separation of the attractive potentials from two surfaces. Accordingly, the primary peaks of the density profiles decrease. For $H = 28.5 \text{ \AA}$, bulk scCO_2 occurs in the central area of the nanochannel apart from the four adsorption layers. The density peaks further decrease because the attractive potentials from two surfaces have been effectively separated into two single potential system. A similar phenomenon can be observed as H further increases from 35.5 \AA to 50 \AA . The results show that nanochannel size has a significant influence on the adsorption

mechanism of scCO_2 especially in very narrow channels. For narrower nanochannels, the superposition of attractive potentials from two surfaces results in strong adsorption of scCO_2 on the surfaces. This can reduce the permeability of scCO_2 in shale porous medium, which contributes to CO_2 storage rather than its flow in shale reservoirs.

Fig. 6(b) shows the residence autocorrelation functions, $C_R(t)$, as a function of the residence time of scCO_2 molecules remaining near the surface. As H increases, $C_R(t)$ decays fast, implying the shorter time that scCO_2 remains in the adsorbed layer. As H increases, the overlapping attractive potentials from two surfaces gradually separate from each other and finally form two single potential systems near the surfaces. This weakens the interaction between scCO_2 and the surfaces resulting in the shorter residence time of scCO_2 on the surface, and also implies a more frequent exchange of scCO_2 appeared between the adsorption layer and bulk phase in the center of nanochannel inside the wider nanochannel. For $H = 7.25 \text{ \AA}$, $C_R(t)$ always equals to one indicating that all scCO_2 molecules reside in the adsorption layer. As H further increases from 14.5 \AA to 50.0 \AA , $C_R(t)$ plateaus appears after about 120 ps indicating that a part of scCO_2 molecules always reside near the surface within the simulation time. Value of $C_R(t)$ plateaus decrease as H increases, also showing the stronger adsorption for narrower nanochannels. As H ranges from 35.5 \AA to 50.0 \AA , $C_R(t)$ curves are basically coincident, suggesting that scCO_2 adsorption is independent of H larger than 35.5 \AA . This is mainly due to that attractive potentials from two surfaces have been effectively divided into two single potential systems near the channel surface. The results also demonstrate that the narrower nanochannel storages CO_2 more securely while the wider nanochannel favors scCO_2 transport.

3.2.2 Effect of nanochannel width on diffusion coefficient of scCO_2 . Fig. 7 demonstrated the dependence of the diffusion coefficient on H . The diffusion coefficient increase monotonically with H , indicating that scCO_2 molecules migrate more easily in wider channels. Compared to the less constraint of bulk phase with a larger diffusion coefficient, the adsorption phase experience a stronger constraint from the surfaces which leads to a smaller diffusion coefficient. The order of diffusibility for scCO_2 at different areas in the nanochannel is bulk phase > second adsorption layer > first adsorption layer, as described in Fig. 7. The diffusion coefficient of scCO_2 molecules in the first adsorption layer is nonzero, which may indicate that the surface diffusion occurs by hopping of scCO_2 molecules from one site to another.⁶¹ Therefore, surface diffusion is one factor that scCO_2 molecules move more quickly in the nanochannel. This mainly results from two aspects. One is the decrease of scCO_2 adsorption density (Fig. 6(a)), leading to the viscosity reduction. The other is the increase of scCO_2 velocity gradient (the inset in Fig. 8(b)), indicating the enhancement of shear effect and then results in the shear thinning, which reduces scCO_2 viscosity.

3.2.3 Effect of nanochannel width on flow behavior of scCO_2 . To understand the effect of nanochannel width on scCO_2 flow behavior, the velocity profiles and the slip lengths were plotted in Fig. 8(a) and (b), respectively. The related fitting

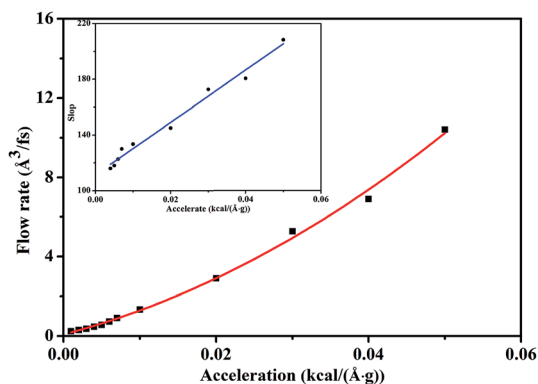


Fig. 5 The flow rate as a function of the external acceleration for scCO_2 molecular.



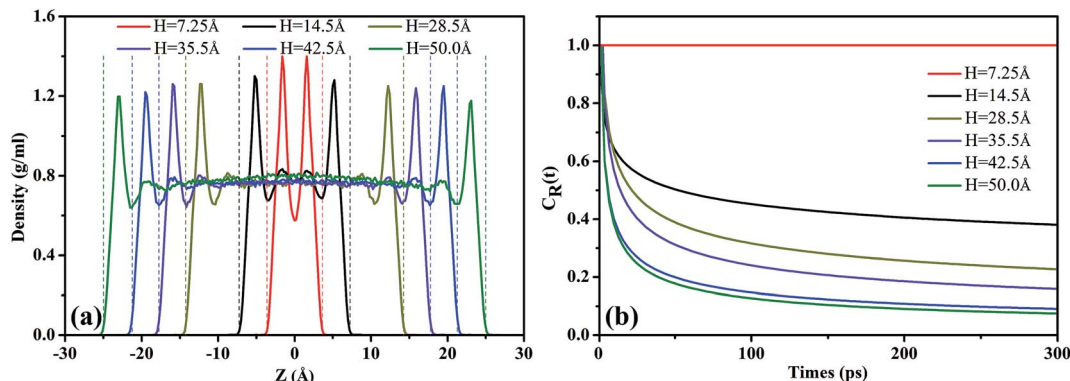


Fig. 6 Adsorption of scCO_2 (a) density profiles of scCO_2 in different width of nanochannel ranging from 7.25 Å to 50.00 Å with acceleration of $0.01 \text{ kcal} (\text{Å}^{-1} \text{g}^{-1})$. (b) Residence autocorrelation function for carbon atoms in the adsorbed layers as a function of time.

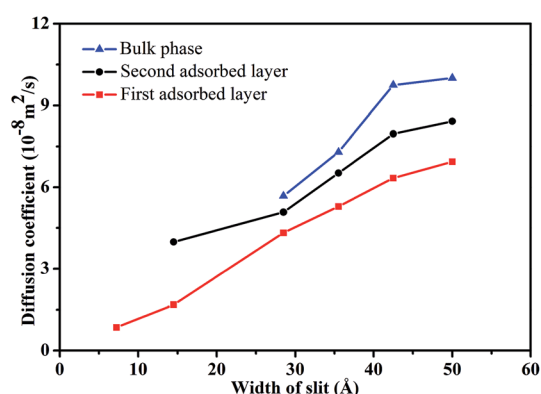


Fig. 7 The diffusion coefficient of scCO_2 molecular in different adsorbed layers behind various width of nanochannel.

parameters describing the flow process were provided in the ESI Table S5.†

In Fig. 8(a), the scCO_2 velocity profiles exhibit a parabolic shape and are symmetrical about the central axis of the nanochannel. Moreover, as H increases, the velocity curve becomes sharper and the axial velocity of scCO_2 increased. This is caused by the intensive constraint on the scCO_2 molecules near the

surface in the smaller nanochannel, as shown in Fig. 6. However, the bulk scCO_2 in the central area of the wider nanochannel are rare constrained.

In Fig. 8(b), the slip length exhibits non-monotonous increase with a maximum value as H increases. For $7.25 \text{ Å} < H < 14.5 \text{ Å}$, the slip velocity increases fast while the velocity gradient increment is small as H expands, as indicated by the inset in Fig. 8(b). Then the ratio of the slip velocity to the velocity gradient, *i.e.*, slip length, increases rapidly. For $14.5 \text{ Å} < H < 28.5 \text{ Å}$, both the slip velocity and the velocity gradient increase rapidly. Ratio of slip velocity to velocity gradient enhances gradually and reaches the maximum value as $H = 28.5 \text{ Å}$. Therefore, the slip length increases slowly and its maximum value occurs. For $35.5 \text{ Å} < H < 50.0 \text{ Å}$, the increase of the slip velocity becomes slower while the velocity gradient increase rapidly. The ratio of them weakens gradually. Consequently, the slip length decreases slowly.

Fig. 8(b) also shows a negative slip length^{54–57} occurring at H less than about 10.0 Å . In this case, the overlapping between attractive potentials from the surfaces is so strong that a part of scCO_2 molecules stick on the surfaces. The external pressure gradient cannot completely overcome the attractive interactions between scCO_2 and the surface. This leads to the zero velocity near the surfaces, indicated the presence of scCO_2 in boundary layer.

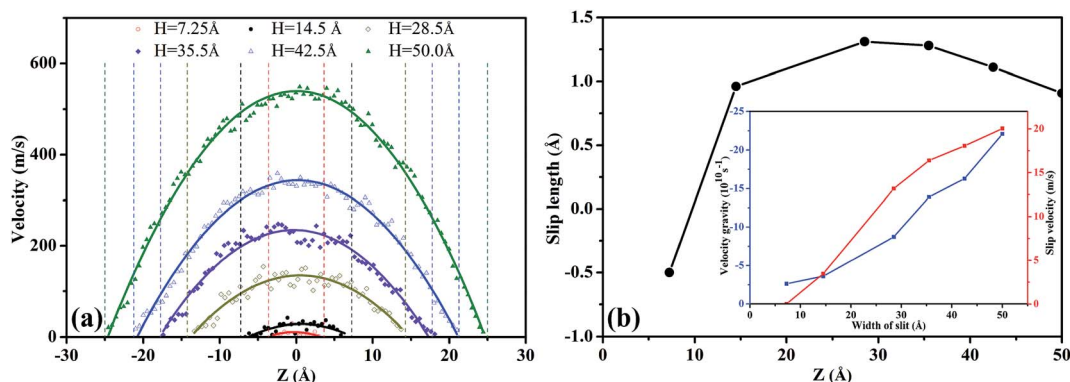


Fig. 8 (a) Effect of nanochannel width on the velocity profiles of scCO_2 . (b) Slip length as a function of the nanochannel width for scCO_2 molecular.



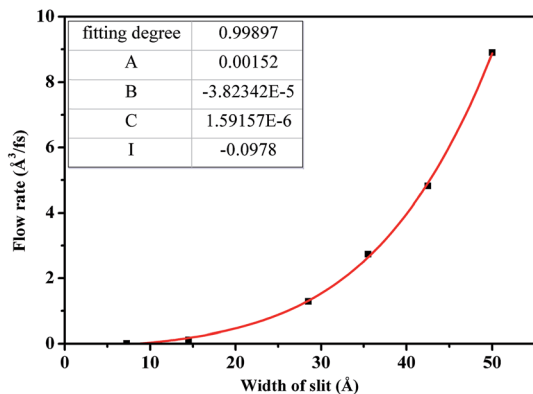


Fig. 9 The dependence of flow rate on channel width for scCO₂ molecular.

Fig. 9 describes the dependence of flow rate on H . As H is less than 30.0 Å, flow rate increases slowly due to the strong constraint on scCO₂ molecules from the superimposition of attractive potentials of two surfaces. The attractive potential from the surface has a significant effect on scCO₂ transport through nanochannel. As H is larger than 30.0 Å, flow rate increases rapidly because of the less constraint on scCO₂ molecules where attractive potentials from two surfaces separate completely. Here, the attractive potential from the surface has little effect on the transport of scCO₂ in nanochannel. Therefore, nanochannels with H less than 30.0 Å contribute to CO₂ storage in shale. To quantitatively describe the dependence of the flow rate on H , the relationship between them was obtained by fitting data applying the power function polynomial

$$Q = AH^2 + BH^3 + CH^4 + I \quad (5)$$

The fitting parameters were shown by the inset in Fig. 9. Compared to the continuum flow with slip effect,⁵² the fourth power of H appears in the fitted formula. This could be mainly due to the fact that both the viscosity and the slip length of scCO₂ in nanochannel relate to H , as indicated in Fig. 7 and 8(b).

4. Conclusions

NEMD simulations were employed to study the scCO₂ transport behavior within the silica nanochannel in shale. The influences of flow driving pressure gradient and nanochannel size were systematically investigated. These effects were understood by exploring density distribution of scCO₂ molecules, residence time of scCO₂ in the first adsorption layer, the diffusion coefficient, the velocity profile, the slippage effect, and the flow rate.

Our simulations reveal that the structuring adsorption layers of scCO₂ molecules occur within the silica nanochannel yet under the driving of pressure gradient. As either pressure gradient or nanochannel width increases, the peaks of scCO₂ density profiles decrease and the density of the bulk phase increases. The higher pressure gradients result in the larger

shear force, which leads to desorbing scCO₂ molecules near the nanochannel surfaces. The wider nanochannel leads to the weaker overlapping of the attractive potentials from the two surfaces, attenuating the adsorption of scCO₂ molecules near the surfaces. The higher pressure gradients and the wider nanochannel can promote scCO₂ diffusibility for both bulk region and the adsorption layers near the surfaces. The improvement of scCO₂ diffusion ability may be mainly determined by the decrease of partial pressure near the surfaces, the increase of velocity of the central area in the nanochannel, and the surface diffusion of scCO₂ hopping from one site to another. The increased diffusion ability also indicates the reduction in scCO₂ viscosity. The negative slippage occurs at lower pressure gradients or within the narrower nanochannel is mainly due to the stronger adsorption of scCO₂ molecules near the surfaces. The slip length exhibits non-monotonic increase and existence of a maximum value with the increase in the pressure gradient or the nanochannel size. The flow rate of scCO₂ through the nanochannel shows a nonlinear characteristic with pressure gradient or nanochannel size. It is also found that the mobility is proportional to the pressure gradient. This implies the breakdown of Darcy's law at nanoscale because of the strong adsorption effect, surface diffusion and slippage effect.

Associated content

Additional simulation results to determine the initial state of scCO₂ in channel, parameters of force field and a part of fitting parameters are described in the text.

Conflicts of interest

There are no conflicts to declare.

Acknowledgements

This work is financially supported by PetroChina Innovation Foundation (2017D-5007-0206) and National Basic Research Program of China (2014CB239204) and the Fundamental Research Funds for the Central Universities (15CX08003A 16CX02052A) and Natural Science Foundation of China (NSFC) (61605251).

References

- 1 H. Wang, G. Li and Z. Shen, *Energy Sources, Part A*, 2012, **34**, 1426–1435.
- 2 Y. Li, H. Nie and P. Long, *Nat. Gas Ind.*, 2009, **12**, 40.
- 3 R. S. Middleton, J. W. Carey, R. P. Currier, J. D. Hyman, Q. Kang, S. Karra, J. Jiménez-Martínez, M. L. Porter and H. S. Viswanathan, *Appl. Energy*, 2015, **147**, 500–509.
- 4 K. Edlmann, S. Haszeldine and C. McDermott, *Environ. Earth Sci.*, 2013, **70**, 3393–3409.
- 5 C. Doughty and K. Pruess, *Vadose Zone J.*, 2004, **3**, 837–847.
- 6 S. A. Hosseini, S. A. Mathias and F. Javadpour, *Transp. Porous Media*, 2012, **94**, 795–815.



- 7 G. R. Van der Werf, D. C. Morton, R. S. DeFries, J. G. Olivier, P. S. Kasibhatla, R. B. Jackson, G. J. Collatz and J. T. Randerson, *Nat. Geosci.*, 2009, **2**, 737–738.
- 8 K. Paustian, O. Andr en, H. H. Janzen, R. Lal, P. Smith, G. Tian, H. Tiessen, M. v. Noordwijk and P. L. Woomer, *Soil Use Manage.*, 1997, **13**, 230–244.
- 9 J. Gibbins and H. Chalmers, *Energy Policy*, 2008, **36**, 4317–4322.
- 10 W. D. Nordhaus, *Econ. J.*, 1991, **101**, 920–937.
- 11 R. W. Howarth, R. Santoro and A. Ingraffea, *Clim. Change*, 2011, **106**, 679.
- 12 J. D. Walls and S. Sinclair, *First Break*, 2011, **29**, 97–101.
- 13 A. H. Kohli and M. D. Zoback, *J. Geophys. Res.: Solid Earth*, 2013, **118**, 5109–5125.
- 14 C. R. Clarkson, N. Solano, R. Bustin, A. Bustin, G. Chalmers, L. He, Y. B. Melnichenko, A. Radliński and T. P. Blach, *Fuel*, 2013, **103**, 606–616.
- 15 M. G. Little and R. B. Jackson, *Environ. Sci. Technol.*, 2010, **44**, 9225–9232.
- 16 R. Leuning, D. Etheridge, A. Luhan and B. Dunse, *Int. J. Greenhouse Gas Control*, 2008, **2**, 401–414.
- 17 A. A. Chialvo, L. Vlcek and D. R. Cole, *J. Phys. Chem. C*, 2012, **116**, 13904–13916.
- 18 H. Wu, J. Chen and H. Liu, *J. Phys. Chem. C*, 2015, **119**, 13652–13657.
- 19 S. Bhatia, K. Tran, T. Nguyen and D. Nicholson, *Langmuir*, 2004, **20**, 9612–9620.
- 20 S. Samios, A. Stubos, N. Kanellopoulos, R. Cracknell, G. Papadopoulos and D. Nicholson, *Langmuir*, 1997, **13**, 2795–2802.
- 21 A. Vishnyakov, P. I. Ravikovitch and A. V. Neimark, *Langmuir*, 1999, **15**, 8736–8742.
- 22 L. Liu and S. K. Bhatia, *J. Phys. Chem. C*, 2013, **117**, 13479–13491.
- 23 M. Firouzi and J. Wilcox, *J. Chem. Phys.*, 2013, **138**, 064705.
- 24 S. Wang, F. Javadpour and Q. Feng, *Fuel*, 2016, **181**, 741–758.
- 25 X. Yang and C. Zhang, *Chem. Phys. Lett.*, 2005, **407**, 427–432.
- 26 Z. Jin and A. Firoozabadi, *Fluid Phase Equilib.*, 2013, **360**, 456–465.
- 27 T. Le, A. Striolo and D. R. Cole, *J. Phys. Chem. C*, 2015, **119**, 15274–15284.
- 28 C. Duan, F. Zhou, K. Jiang and T. Yu, *Int. J. Heat Mass Transfer*, 2015, **91**, 1088–1100.
- 29 B. Liu, C. Wang, J. Zhang, S. Xiao, Z. Zhang, Y. Shen, B. Sun and J. He, *Energy Fuels*, 2017, **31**, 738–746.
- 30 C. R. Clarkson, M. Nobakht, D. Kaviani and T. Ertekin, *SPE J.*, 2012, **17**, 230–242.
- 31 S. Sinha, E. Braun, M. Determan, Q. Passey, S. Leonardi, J. Boros, A. Wood Iii, T. Zirkle and R. Kudva, *Steady-State Permeability Measurements on Intact Shale Samples at Reservoir Conditions – Effect of Stress, Temperature, Pressure, and Type of Gas*, 2013, DOI: 10.2118/164263-MS.
- 32 K. Falk, B. Coasne, R. Pellenq, F.-J. Ulm and L. Bocquet, *Nat. Commun.*, 2015, **6**, 6949.
- 33 P. J. Monteiro, C. H. Rycroft and G. I. Barenblatt, *Proc. Natl. Acad. Sci.*, 2012, **109**, 20309–20313.
- 34 E. R. Cruz-Chu, A. Aksimentiev and K. Schulten, *J. Phys. Chem. B*, 2006, **110**, 21497–21508.
- 35 M. Kazemi and A. Takbiri-Borujeni, *Energy Fuels*, 2016, **30**, 8156–8163.
- 36 A. Botan, V. Marry, B. Rotenberg, P. Turq and B. Noetinger, *J. Phys. Chem. C*, 2013, **117**, 978–985.
- 37 B. Liu, R. Wu, J. A. Baimova, H. Wu, A. W.-K. Law, S. V. Dmitriev and K. Zhou, *Phys. Chem. Chem. Phys.*, 2016, **18**, 1886–1896.
- 38 S. Wang, F. Javadpour and Q. Feng, *Fuel*, 2016, **171**, 74–86.
- 39 S. Plimpton, *J. Comput. Phys.*, 1995, **117**, 1–19.
- 40 W. Humphrey, A. Dalke and K. Schulten, *J. Mol. Graphics*, 1996, **14**, 33–38.
- 41 G. J. Martyna, D. J. Tobias and M. L. Klein, *J. Chem. Phys.*, 1994, **101**, 4177–4189.
- 42 N. Shuichi, *Prog. Theor. Phys. Suppl.*, 1991, **103**, 1–46.
- 43 I. C. Bourg and C. I. Steefel, *J. Phys. Chem. C*, 2012, **116**, 11556–11564.
- 44 J. G. Harris and K. H. Yung, *J. Phys. Chem.*, 1995, **99**, 12021–12024.
- 45 R. Hockney, S. Goel and J. Eastwood, *J. Comput. Phys.*, 1974, **14**, 148–158.
- 46 T. Wu and D. Zhang, *Sci. Rep.*, 2016, **6**, 23629.
- 47 D. Kasiteropoulou, T. E. Karakasidis and A. Liakopoulos, *J. Mater. Sci. Eng. B*, 2011, **176**, 1574–1579.
- 48 D. Argyris, N. R. Tummala, A. Striolo and D. R. Cole, *J. Phys. Chem. C*, 2008, **112**, 13587–13599.
- 49 Y. Zhang, Y. Zhu, Z. Li, Y. Ruan, L. Li, L. Lu and X. Lu, *Fluid Phase Equilib.*, 2016, **430**, 169–177.
- 50 L. Guzzardi, D. Cazar, C. del Hierro, F. Torres and M. M endez, *Theor. Chem. Acc.*, 2016, **135**, 1–6.
- 51 R. Roque-Malherbe, R. Polanco-Estrella and F. Marquez-Linares, *J. Phys. Chem. C*, 2010, **114**, 17773–17787.
- 52 Z. Jin and A. Firoozabadi, *J. Chem. Phys.*, 2015, **143**, 104315.
- 53 L. Bocquet and J.-L. Barrat, *Soft Matter*, 2007, **3**, 685–693.
- 54 E. Bonaccorso, H.-J. Butt and V. S. Craig, *Phys. Rev. Lett.*, 2003, **90**, 144501.
- 55 J. Hyv aluoma and J. Harting, *Phys. Rev. Lett.*, 2008, **100**, 246001.
- 56 G. McHale and M. Newton, *J. Appl. Phys.*, 2004, **95**, 373–380.
- 57 A. Author, *Lab Chip*, 2007, **7**, 299–301.
- 58 Y. Gratton and G. Slater, *Eur. Phys. J. E: Soft Matter Biol. Phys.*, 2005, **17**, 455–465.
- 59 H. Yu, J. Chen, Y. Zhu, F. Wang and H. Wu, *Int. J. Heat Mass Transfer*, 2017, **111**, 1172–1180.
- 60 M. Makaremi, K. D. Jordan, G. D. Guthrie and E. M. Myshakin, *J. Phys. Chem. C*, 2015, **119**, 15112–15124.
- 61 A. Berezhkovskii and G. Hummer, *Phys. Rev. Lett.*, 2002, **89**, 064503.

